

Electronic Supplementary Material for

Enhancing corannulene chemiluminescence, electrochemiluminescence and photoluminescence by means of an azabora-helicene to slow down its bowl inversion

Xiaoli Qin,^{a,b||} Lin Huang,^{c,d,e||} Ziyang Zhan,^{a||} Peng Fu,^{c,d,e} Qing Wang,^{c,f} Congyang Zhang,^a
Jianhui Huang^{c,d,e,*} and Zhifeng Ding^{a,*}

^a *Department of Chemistry, Western University, London, ON N6A 5B7, Canada*

^b *College of Chemistry and Material Science, Hunan Agricultural University, Changsha 410128, China*

^c *School of Pharmaceutical Science and Technology, Faculty of Medicine, Tianjin University, Tianjin 300072, China*

^d *International Center of Chemical Science and Engineering, Tianjin 300072, China*

^e *International Joint Research Centre for Molecular Sciences, Tianjin University, Tianjin 300072, China*

^f *National Institute of Biological Sciences, No. 7 Science Park Road, Zhongguancun Life Science Park, Beijing 102206, China*

||X. Qin, L. Huang and Z. Zhan contributed equally to this work.

Experimental Section

1. Materials and General methods

Reagents: Sodium salicylate ($\geq 99.5\%$), bis(2-carbopentyloxy-3,5,6-trichlorophenyl) oxalate (CPPO, $\geq 96.5\%$), *N,N*-dimethylformamide (DMF, $\geq 99.8\%$), tripropylamine (TPrA, $\geq 98\%$), benzoyl peroxide (BPO, $\geq 98\%$), tetrabutylammonium hexafluorophosphate (TBAPF₆, $\geq 99.0\%$), benzene (99.8%), acetonitrile ($\geq 99.9\%$) and ferrocene (Fc, 98%) were purchased from Sigma-Aldrich Canada. Hydrogen peroxide (H₂O₂, 30%) was bought from Thermo Fisher Scientific (Canada) and used as received.

Syntheses: Unless otherwise stated, all chemicals were reagent-grade or higher, obtained from commercial sources, and used for synthesis without further purification. Flash chromatography was performed on silica gel 200-300 mesh. Thin layer chromatography (TLC) was performed on glass-backed plates that were pre-coated with silica (GF254) and developed using standard visualizing agents.

NMR Spectroscopy: ¹H and ¹³C NMR spectra were recorded on a 400 MHz or 600 MHz BRUKER AVANCE spectrometer at 298 K. Chemical shifts (δ) are reported in ppm with the solvent resonance as the internal standard (CDCl₃ ¹H: δ 7.26, ¹³C: δ 77.16; CD₂Cl₂ ¹H: δ 5.32, ¹³C: δ 53.84). Data are reported as follows: chemical shift, multiplicity (s = singlet, d = doublet, t = triplet, q = quartet, br = broad, m = multiplet), integration, coupling constants (*J*) in Hz.

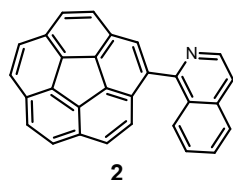
Mass Spectrometry: High-resolution mass spectra (HRMS) recorded for accurate mass analysis were performed on a Q-TOF micro (Bruker Compass Data Analysis 4.0) spectrometer.

X-ray structure analysis: X-ray structure analyses were carried out by Rigaku, XtaLAB FRX in the Instrumental Analysis Center, School of Pharmaceutical Science and Technology, Tianjin University.

2. Synthesis and Characterization

Cor-Bpin was prepared according to literature procedures.¹

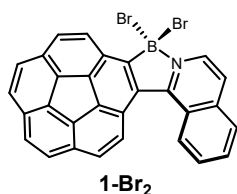
2.1 Synthesis of 2-isoquinolinecorannulene (**2**)



To a solution of 1-chloroisoquinoline **IQ-Cl** (70 mg, 0.33 mol, 1.1 equiv.) in DME (2.5 mL) under an inert atmosphere was added a solution of Corannulene boronic acid ester (**Cor-Bpin**) (113 mg, 0.3 mmol, 1.0 equiv.) in MeOH (0.75 mL) followed by a solution of Na₂CO₃ (95 mg, 0.9 mmol, 3.0 eq.) in water (0.85 mL). The mixture was degassed and subsequently, Pd(PPh₃)₄ (10 mg, 9.0 μmol, 0.03 eq.) was added. The reaction mixture was heated up to 85 °C for overnight. Afterwards, the reaction mixture was brought to room temperature, diluted with water, and extracted with EtOAc (10 ml × 3). The combined organic layers were washed with water and brine, dried over Na₂SO₄, and filtered, and the solvent was removed under reduced pressure. The crude product was purified by flash column chromatography (silica, hexane/EtOAc 8:2) to obtain desired compound **2** (93 mg, 82%) as a solid. **m.p.** 199–200 °C. ¹H NMR (400 MHz, CDCl₃) δ = 8.72 (d, *J* = 5.7 Hz, 1H, ArH), 8.20 (d, *J* = 6.2 Hz, 1H, ArH), 8.11 (s, 1H, ArH), 7.97 (d, *J* = 8.3 Hz, 1H, ArH), 7.88 (dd, *J* = 11.4 Hz 2H, ArH), 7.85–7.83

(m, 3H, ArH), 7.79 (d, $J = 8.8$ Hz, 1H, ArH), 7.78 (d, $J = 5.2$ Hz, 1H, ArH), 7.73 (t, $J = 7.0$ Hz, 1H, ArH), 7.68 (d, $J = 8.9$ Hz, 1H, ArH), 7.50 (t, $J = 7.6$ Hz, 1H, ArH), 7.41 (d, $J = 8.9$ Hz, 1H, ArH). ^{13}C NMR (101 MHz, CDCl_3) $\delta = 159.2, 142.6, 138.4, 136.8, 136.4, 136.1, 135.9, 135.8, 131.3, 131.1, 131.0, 130.7, 130.6, 130.4, 129.1, 128.3, 128.2, 127.5, 127.5, 127.5, 127.4, 127.4, 127.4, 127.3, 127.2, 127.1, 126.7, 120.5$. A carbon signal was missed in ^{13}C NMR spectrum, possibly due to overlap of peaks. IR (KBr) ν [cm^{-1}] 3192, 3182, 3045, 3028, 1580, 1554, 1385, 1351, 1314, 827, 749, 660, 551. HRMS (ESI) m/z calcd for $\text{C}_{29}\text{H}_{16}\text{N}$ $\{[\text{M}+\text{H}]^+\}$ 378.1283, found 378.1279.

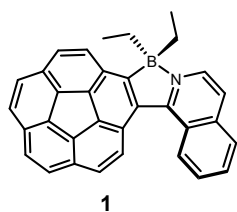
2.2 Synthesis of 1-Br₂



2-isoquinolinecorannulene **2** (88 mg, 0.23 mmol, 1.0 eq.) was dissolved in CH_2Cl_2 (2.4 mL), and $i\text{-Pr}_2\text{NEt}$ (40 μL , 0.23 mmol, 1.0 equiv.) was added under an inert atmosphere. BBr_3 (68 μL , 0.7 mmol, 176 mg, 3.0 equiv.) was added dropwise at room temperature, and the mixture was stirred for 24 h. Subsequently, the reaction was quenched with saturated aqueous K_2CO_3 solution, and the mixture was diluted with CH_2Cl_2 and distilled water. The phases were separated, and the aqueous phase was extracted with CH_2Cl_2 . The combined organic layers were washed with distilled water and brine, dried over anhydrous Na_2SO_4 , and filtered, and the

volatiles were removed under reduced pressure. The crude product was obtained as a yellow solid and used in the next step without any further purification.

2.3 Synthesis of compound 1



Compound **1-Br₂** (110 mg, 0.2 mmol, 1.0 eq.) was dissolved in a mixture of CH₂Cl₂ (2 mL) and toluene (2 mL), and AlEt₃ (1 M solution in *n*-hexane, 450 μL, 0.45 mmol, 2.2 eq.) was added dropwise under an inert atmosphere. The reaction was stirred for 2 h and subsequently quenched with water. The phases were separated, and the aqueous layer was extracted with CH₂Cl₂. The combined organic layers were washed with distilled water and brine, dried over Na₂SO₄, and filtered, and the solvent was removed under reduced pressure. The crude product was purified via flash chromatography (silica, CH₂Cl₂/hexane 1:9) to obtain compound **1** (60 mg, 67%) as a yellow solid. ¹H NMR (400 MHz, CDCl₃) δ = 9.76 (d, *J* = 9.6 Hz, 1H, ArH), 8.29–8.27 (m, 2H, ArH), 8.13 (d, *J* = 8.8 Hz, 1H, ArH), 8.06–8.03 (m, 1H, ArH), 7.96–7.84 (m, 6H, ArH), 7.81 (d, *J* = 8.7 Hz, 1H, ArH), 7.75 (d, *J* = 8.8 Hz, 1H, ArH), 7.74 (d, *J* = 6.1 Hz, 1H, ArH), 1.20–1.14 (m, 2H, CH₂), 1.00–0.91 (m, 2H, CH₂), 0.19 (br, 6H, CH₃). ¹³C NMR (101 MHz, CDCl₃) δ = 158.3, 137.9, 137.7, 136.3, 136.0, 135.3, 133.6, 132.8, 132.6, 132.2, 131.0, 130.6, 129.8, 129.4, 128.5, 128.1, 127.6, 127.5, 127.4, 127.0, 126.9, 126.9, 126.8, 126.8, 125.0, 119.1, 10.2. Signals corresponding to the C atoms bound to the B atom are not visible.

^{11}B NMR (128 MHz, CDCl_3) $\delta = 3.2$ ppm. HRMS (ESI) m/z calcd for $\text{C}_{37}\text{H}_{27}\text{BN}$ $\{[\text{M}+\text{H}]^+\}$ 496.2236, found 496.2231.

3. Electrochemical and ECL Measurements

The electrochemistry and ECL experiments were carried out using an Autolab potentiostat (PGSTAT30, Metrohm, Switzerland) with a conventional three-electrode system. The working electrode was a Pt disk electrode embedded in a soft glass tubing with a diameter of 2 mm, while the counter electrode and reference electrode were Pt wire coils. The working electrode and the ECL cell were cleaned as previously reported elsewhere by us.^{2, 3} In a N_2 -filled glovebox, ECL experiments were performed in a 0.6 mM Cor or **1** solution of 1:1 (volume ratio) benzene:acetonitrile (benzene:MeCN) with 0.1 M TBAPF₆ as the supporting electrolyte. The ECL detector was a calibrated photomultiplier tube (PMT, R3896, Hamamatsu, Japan) biased at a high-voltage of -750 V, collecting the ECL-voltage curves under the flat Pyrex window at the bottom of the cell (Figure S1A). The ECL signal in the format of photocurrent from the PMT was transformed into a voltage signal by a scale-adjustable picoammeter (Keithley 6487, Cleveland, OH). The ECL units were nA or μA . All potentials in this paper were calibrated to that of the saturated calomel electrode (SCE) using ferrocenium/ferrocene (Fc^+/Fc) as the internal reference ($E_{\text{Fc}^+/\text{Fc}}^0 = 0.342$ V vs. SCE).⁴

4. ECL and PL Spectroscopy Measurements:

ECL spectra were measured as reported elsewhere⁵ by a spectrograph with a grating of

50 l/mm blazed at 600 nm (Acton 2300i, Teledyne Princeton Instruments, MA) coupled with a charge coupled device (CCD) camera (Model DU401- BR-DD-352, Andor Technology, UK) being cooled at $-65\text{ }^{\circ}\text{C}$. An electrochemical workstation (CHI 610A, CH Instruments, Austin, TX) was used to drive the electrochemical reactions during spectroscopic measurements (Figure S7B). The units of the ECL spectra were counts. Before ECL measurement, a commercial mercury-argon source (HG-1, Ocean Insight, Orlando, FL) was used for wavelength calibration. Both accumulated and spooling ECL spectra were collected during potential dynamic scans.

Photoluminescence (PL) spectroscopy experiments were performed in a $10\text{ }\mu\text{M}$ Cor or $5\text{ }\mu\text{M}$ **1** in 1:1 benzene/MeCN solution by a Fluorolog spectrophotometer (QM-7/2005, Photon Technology International, London, ON) with an excitation slit width of 0.25 mm and an emission slit width of 0.1 mm. Absolute PL quantum yields were determined on an Edinburgh FSS Fluorometer (Edinburgh Instruments Ltd., UK) utilizing an integrating sphere.

5. CL Spectroscopy Measurements

All CL measurements for **1** were conducted inside a cylindrical glass tube. The CL spectra were collected using a 6-inch integrating sphere (Labsphere, North Sutton, NH) and spectrometer (USB2000+, Ocean Insight, Orlando, FL), while light travelled through the optical fiber and was detected by the spectrometer (Figure S1C). Light emissions were collected entirely by the integrating sphere diffusing homogeneously and sending a certain amount of the light to the spectrometer through an optical fibre. The light collection is not dependent on CL cell geometry, as long as the light is in the sphere. Calibration of the spectroscopy wavelength

on the spectrometer was performed using a mercury–argon source (model HG-1, Ocean Insight, Orlando, FL).⁵ The individual and spooling CL spectra were acquired and saved with OceanView software (Ocean Insight).

For the CL spectroscopy measurements of **Cor**,⁶ all analyses were conducted inside a cylindrical glass tube. The CL spectra of GQD were collected using a 6-inch integrating sphere (Labsphere, North Sutton, NH) and a charge-coupled device (CCD) camera (iDUS401a-BR-DD, Andor Technologies, Belfast, UK) cooled at -65 °C, attached to a spectrograph (Acton SP2300i, Teledyne Princeton Instruments – Massachusetts, Acton, MA). Calibration of the spectroscopy wavelength was performed using a mercury–argon source (model HG-1, Ocean Insight, Orlando, FL).⁵ All accumulation emission spectra reported in this work have been baseline-corrected by numerical subtraction of an identical duration background scan and intensity-normalized to allow for meaningful comparison. The obtained CL spectra from the spectrograph and CCD camera set-up were calibrated by the Ocean Insight USB2000+ Spectrometer (OIS), which was converted to read in terms of optical power using a calibration lamp (LS-1-CAL-int) along with the integrating sphere. In total, five calibration points were collected by varying the running time of the lamp with 1, 2, 3, 4 and 5 s. These measurements were then repeated on the spectrograph-CCD camera set-up to correlate the OIS optical power readings, in which an optical density filter was used to reduce the radiant power of the lamp down to a scale appropriate for the calibration procedures. The measured CL spectra were interpolated to derive 2048 pixels with an interval value of 0.38 nm in a wavelength range between 341.21 and 1029.64 nm and converted from counts to power values in $\mu\text{W}/\text{nm}$. Total photons were obtained by integration of the power-wavelength curves with the assistance of

custom programs in MATLAB software (Version 2021b, MathWorks Inc., Natick, MA) developed in our group similar to those for determining absolute ECL quantum efficiencies.

Commission International de l'Éclairage (CIE) colour diagrams of CL, ECL, and PL emissions were calculated using a MATLAB program (2021b).

6. Absolute ECL and CL Quantum Efficiencies

The absolute ECL quantum efficiency was determined by comparing the number of photons emitted with the number of electrons injected,^{7,8} as represented in equation (1):

$$\begin{aligned}\Phi_{ECL} &= 100\% \times \frac{\text{total photons}}{\text{total electrons}} = 100\% \times \frac{\int v_{\text{photons}} dt}{\int v_{\text{electrons}} dt} \\ &= 100\% \times \frac{\int PC dt}{\int (|i_x| - |i_{BG}|) dt} \times \frac{N_A \times k_{ABS} \times q_e}{F \times \sigma_{PMT} \times C}\end{aligned}\quad (1)$$

where v_{photons} is the total ECL photon emission rate and $v_{\text{electrons}}$ is the total Faradaic electron rate flowing into the electrochemical cell, yielding total Φ_{ECL} in a percentage of photons per electron. PC is the ECL signal as photocurrent, i_x is the total electrochemical current including Faradaic and non-Faradaic current (i_{BG}), N_A is Avogadro's number, k_{ABS} is the absorption correction factor, q_e is a constant related to the charges per electron, F is Faraday's constant, C is a hardware and wavelength specific factor, and σ_{PMT} is a correction factor related to the PMT surface area, distance from PMT to electrode, and electrode reflectivity.^{7,8} The total photons could be obtained by the integration of PC from the calibrated R3896 PMT with a known responsive curve in the wavelength range and gain factor at its specific high voltage applied.

According to previous reports on peroxyoxalate-based CL systems of organic dyes such as rubrene, rhodamine, and anthracene derivatives,^{9,10} the intensity of the CL reaction depends

solely on the concentration of the high-energy intermediate 1,2-dioxetane, which in turn is limited by the consumption rate of the rate-limiting reagent CPPO. Thus, the CL quantum efficiency (Φ_{CL}) in einsteins per mole is calculated from eq. 2 with the assistance of eqs. 3-4.¹¹,

12

$$\Phi_{CL} = \frac{\text{total photons}}{n_{CPPO} \times 6.02 \times 10^{23}} \times 100\% \quad (2)$$

$$E = \frac{hc}{\lambda} = J \text{ per photon}(\lambda) \quad (3)$$

$$W = \frac{J}{s} \times \frac{1}{\frac{J}{\text{photon}(\lambda)}} = \frac{\text{photon}(\lambda)}{s} \quad (4)$$

where n_{CPPO} is the number of CPPO moles used in the CL reaction, c is the speed of light (3×10^8 ms^{-1}), λ is the individual photon wavelength, J is the energy of an individual photon at a wavelength of λ , and h is Planck's constant (6.626×10^{-34} J·s). The total number of photons emitted by the system for eq. 2 can be determined by integration of the absolute photon response-wavelength curve over the appropriate wavelength range, from which a CL efficiency can be obtained straightforwardly via eq. 2. All of these operations can be performed with OceanView software (Ocean Insight); the results were verified with a custom-made MATLAB program.

^1H , ^{13}C , and ^{11}B NMR Spectra

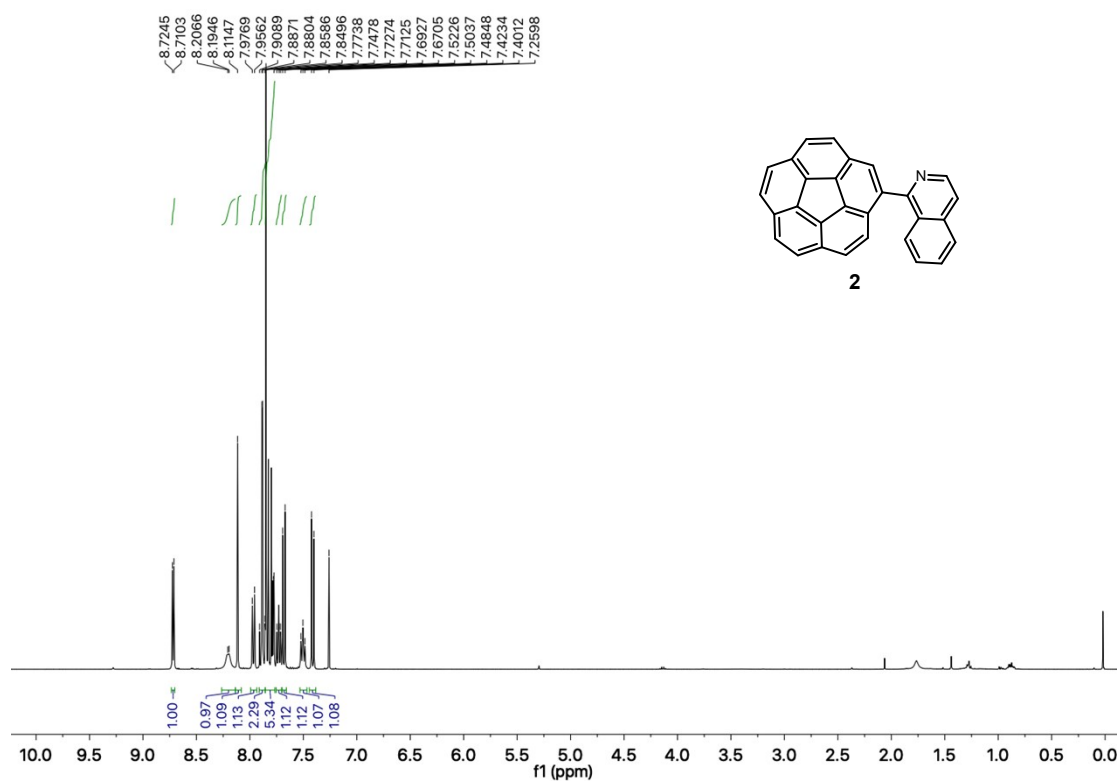


Figure S1 ^1H NMR (400 MHz, CDCl_3) spectrum of 2.

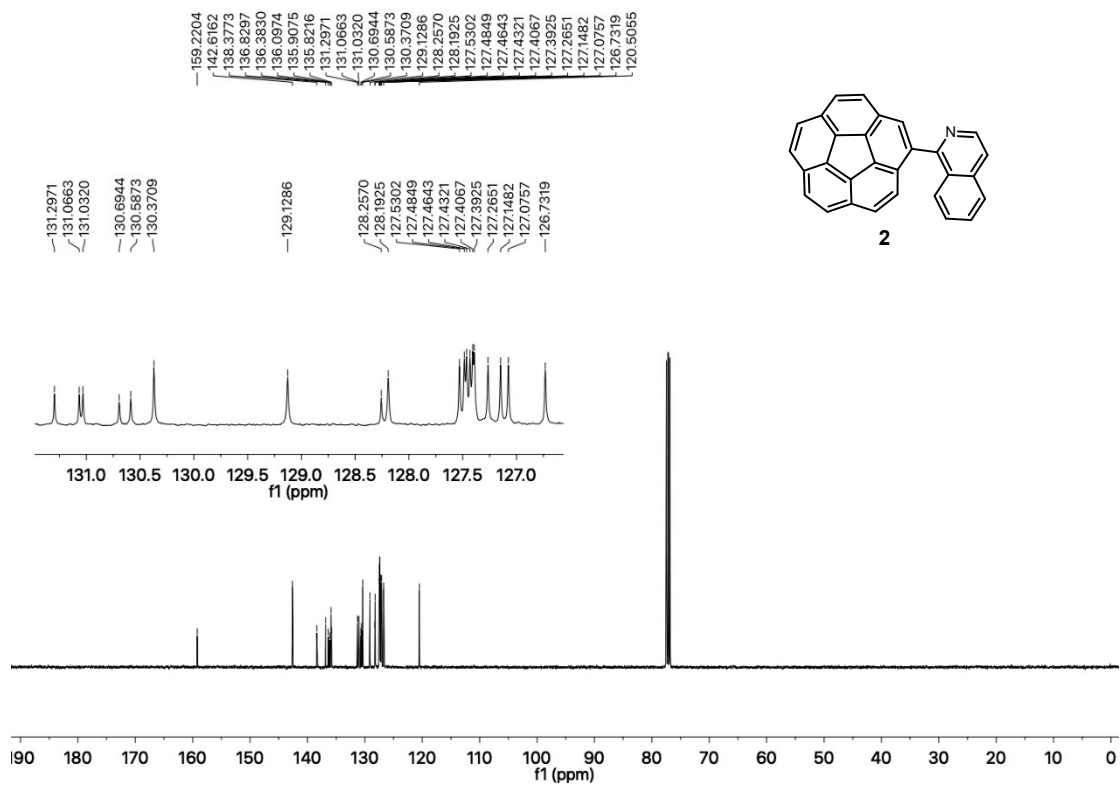


Figure S2 ^{13}C NMR (101 MHz, CDCl_3) spectrum of 2.

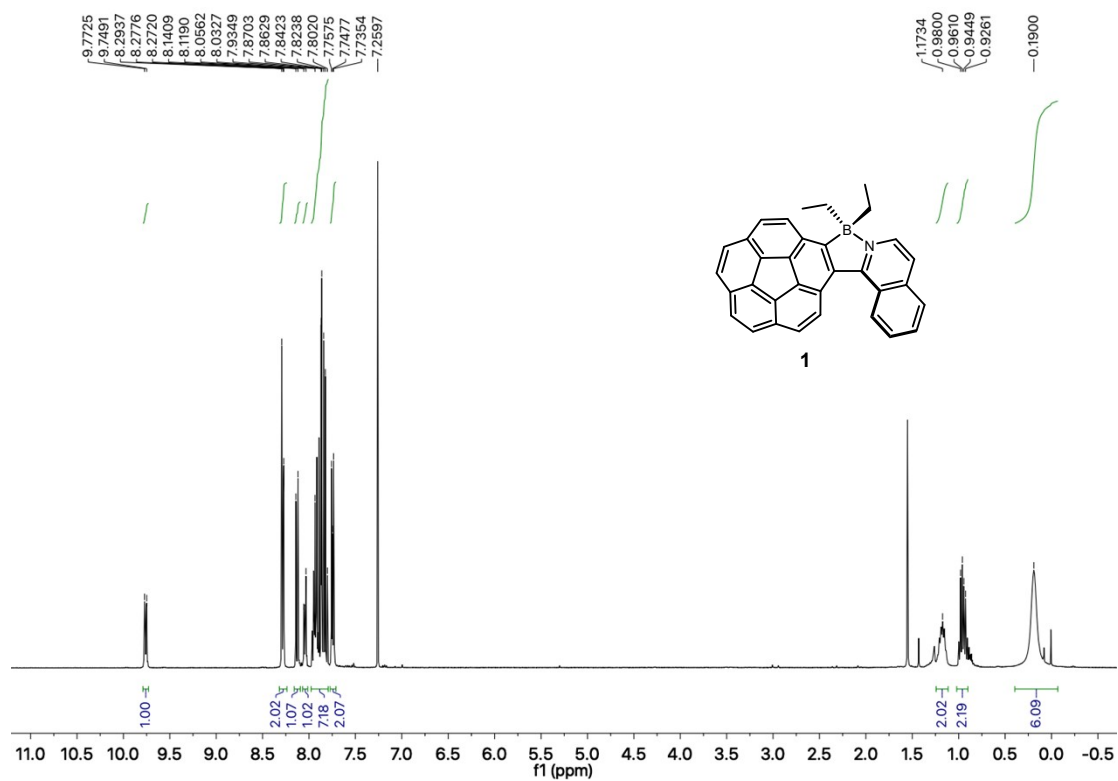


Figure S3 ¹H NMR (400 MHz, CDCl₃) spectrum of **1**.

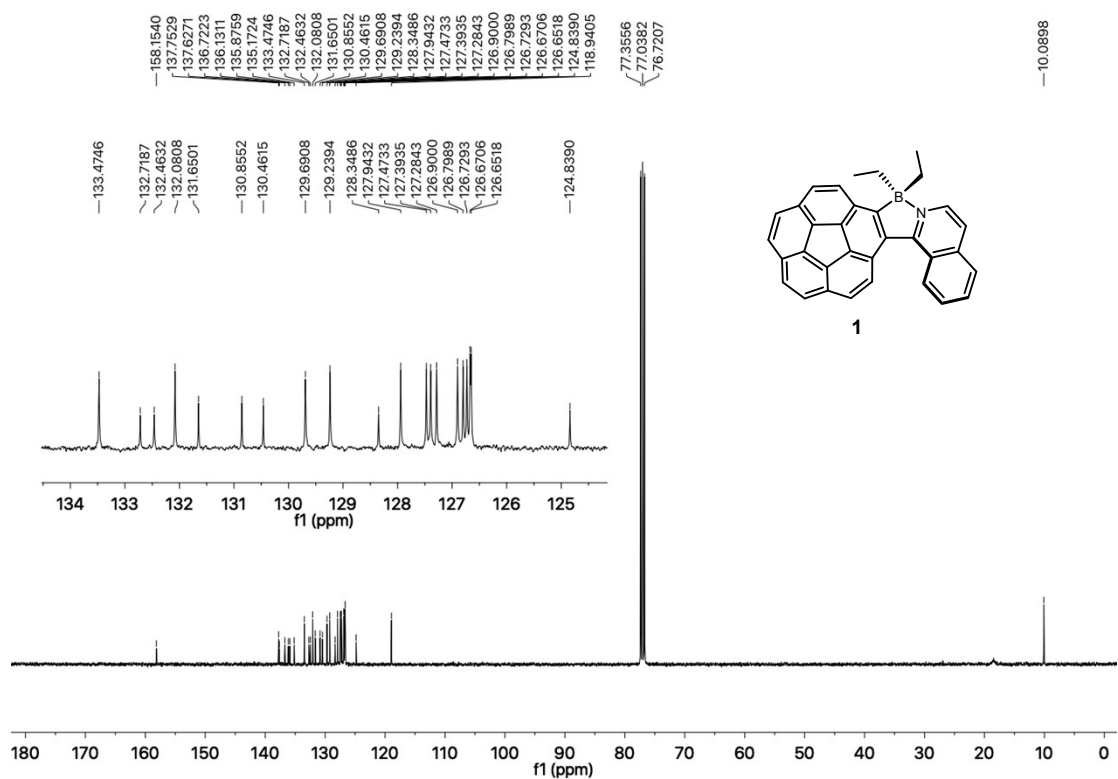


Figure S4 ¹³C NMR (101 MHz, CDCl₃) spectrum of **1**.

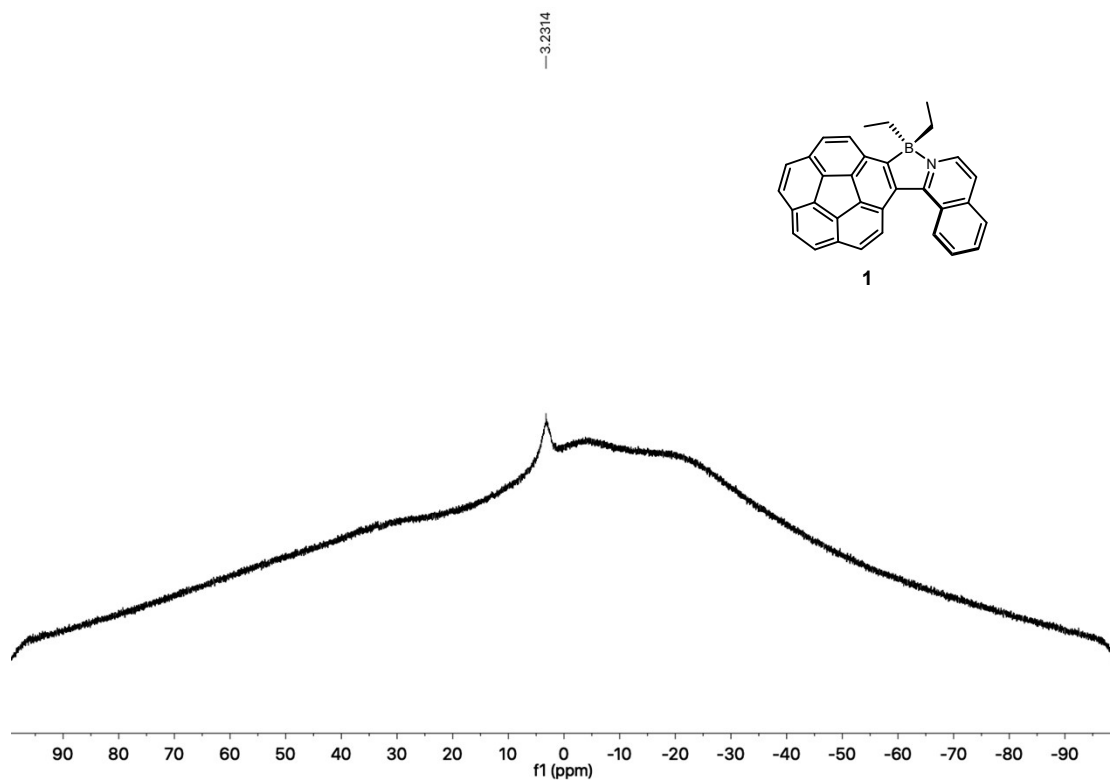


Figure S5 ^{11}B NMR (128 MHz, CDCl_3) spectrum of **1**.

Single Crystal X-ray Analysis

Slow evaporation of a dichloromethane solution at room temperature furnished a yellow block-like racemic crystal of **1**. Single crystal X-ray diffraction data for compound **1** was collected at 160 K on a Rigaku XtaLAB FRX diffractometer equipped with a Hypix6000HE detector using Cu K α radiation ($\lambda=1.54184$ Å). Data were reduced using the software package CrysAlisPro by applying an empirical absorption correction. The structure was solved using direct methods, expanded with Fourier techniques, and refined with SHELXL¹³ in Olex2.¹⁴

Crystal data for 1: C₃₃H₂₄BN, $M_r = 445.34$, yellow block, $0.1 \times 0.07 \times 0.04$ mm³, monoclinic space group P2₁/ n , $a = 8.69340(10)$ Å, $b = 21.4946(4)$ Å, $c = 12.5425(2)$ Å, $\alpha = 90^\circ$, $\beta = 94.2760(10)^\circ$, $\gamma = 90^\circ$, $V = 2337.18(6)$ Å³, $Z = 4$, $\rho_{\text{calc}} = 1.266$ g/cm³, $\mu = 0.547$ mm⁻¹, $F_{(000)} = 936.0$, $T = 160(2)$ K, $\text{Goof}(F^2) = 1.033$, $R_I = 0.0542$, $wR_2 = 0.1578$ for $I \geq 2\sigma(I)$, $R_I = 0.0680$, $wR_2 = 0.1709$ for all data, 4554 independent reflections [$\theta \leq 75.475^\circ$] with a completeness of 98.4% and 318 parameters and 0 restraints.

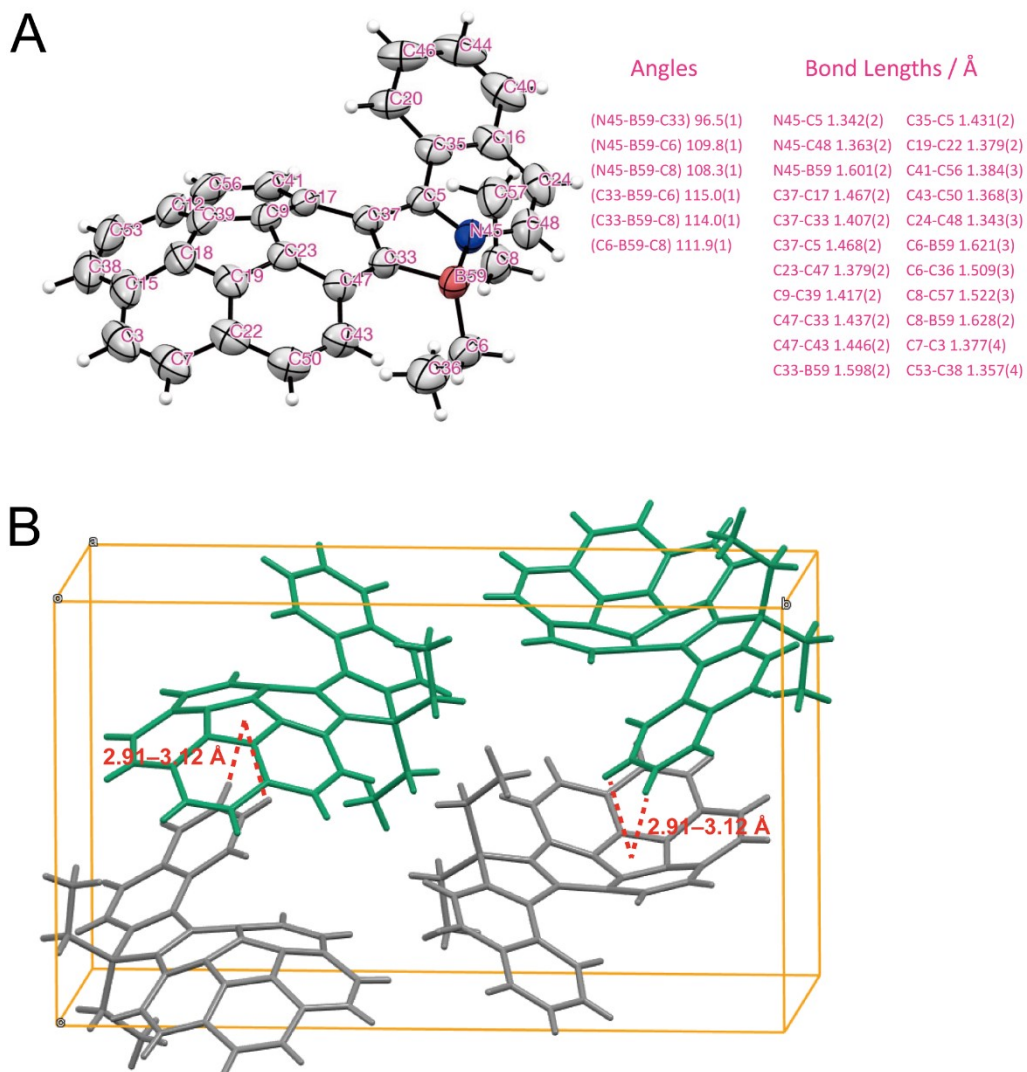


Figure S6 (A) Molecular structure of **1** in the solid state with the selected bond lengths and angles. Thermal displacement parameters are displayed at the 50% probability. (B) Crystal packing unit and C–H··· π interactions (2.91–3.12 Å) between the Ph ring of isoquinoline and corannulene motif. (*P*)- and (*M*)-enantiomers are colored in green and gray, respectively.

Molecular orbital description from DFT calculations

Gaussian 16 (revision B.01) program was utilized for DFT calculations using the B3LYP method with the 6-311G (2d, p) basis set for energy calculations (the solvation model was used with acetonitrile).

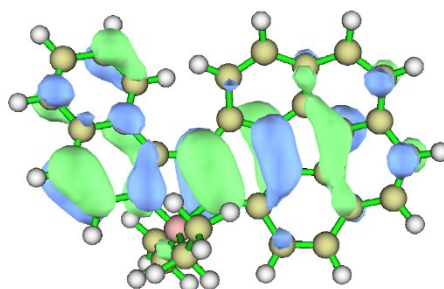
Compound 1:

Orb:	111	Ene(au/eV):	-0.273859	-7.4521	Occ: 2.000000	Type:A+B
Orb:	112	Ene(au/eV):	-0.261729	-7.1220	Occ: 2.000000	Type:A+B
Orb:	113	Ene(au/eV):	-0.253032	-6.8854	Occ: 2.000000	Type:A+B
Orb:	114	Ene(au/eV):	-0.235319	-6.4034	Occ: 2.000000	Type:A+B
Orb:	115	Ene(au/eV):	-0.233397	-6.3511	Occ: 2.000000	Type:A+B
Orb:	116	Ene(au/eV):	-0.231543	-6.3006	Occ: 2.000000	Type:A+B
Orb:	117	Ene(au/eV):	-0.218662	-5.9501	Occ: 2.000000	Type:A+B
Orb:	118	Ene(au/eV):	-0.089715	-2.4413	Occ: 0.000000	Type:A+B
Orb:	119	Ene(au/eV):	-0.070520	-1.9190	Occ: 0.000000	Type:A+B
Orb:	120	Ene(au/eV):	-0.061843	-1.6828	Occ: 0.000000	Type:A+B
Orb:	121	Ene(au/eV):	-0.047443	-1.2910	Occ: 0.000000	Type:A+B
Orb:	122	Ene(au/eV):	-0.019249	-0.5238	Occ: 0.000000	Type:A+B
Orb:	123	Ene(au/eV):	-0.007712	-0.2098	Occ: 0.000000	Type:A+B
Orb:	124	Ene(au/eV):	0.004828	0.1314	Occ: 0.000000	Type:A+B

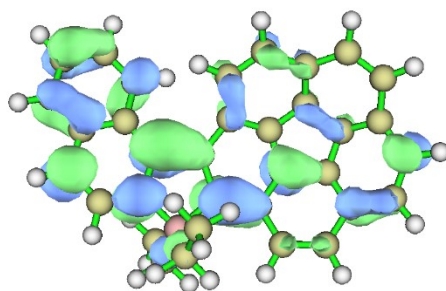
Note: Orbital 117 is HOMO, energy: -0.218662 a.u. -5.950107 eV
Orbital 118 is LUMO, energy: -0.089715 a.u. -2.441276 eV
HOMO-LUMO gap: 0.128947 a.u. 3.508831 eV 338.550847 kJ/mol

Iso_value = 0.03

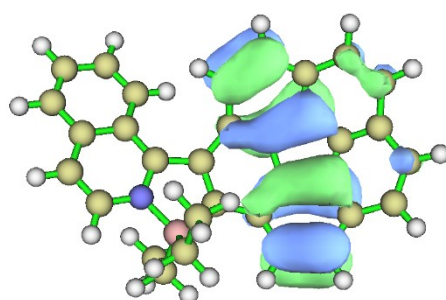
HOMO:



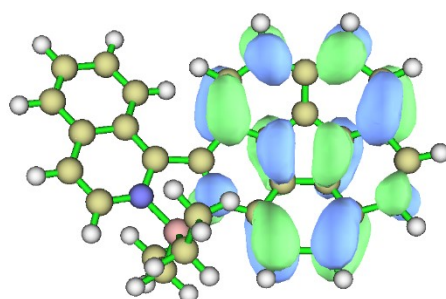
LUMO:



Orbital 116:



Orbital 119:



Pristine Corannulene:

Orb:	50	Ene(au/eV):	-0.405909	-11.0453	Occ: 2.000000	Type:A+B
Orb:	51	Ene(au/eV):	-0.405902	-11.0452	Occ: 2.000000	Type:A+B
Orb:	52	Ene(au/eV):	-0.387317	-10.5394	Occ: 2.000000	Type:A+B
Orb:	53	Ene(au/eV):	-0.381861	-10.3910	Occ: 2.000000	Type:A+B

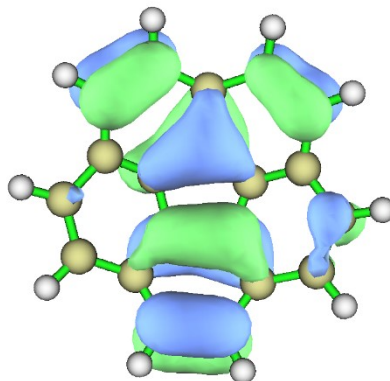
Orb:	54	Ene(au/eV):	-0.381853	-10.3907	Occ: 2.000000	Type:A+B
Orb:	55	Ene(au/eV):	-0.345070	-9.3898	Occ: 2.000000	Type:A+B
Orb:	56	Ene(au/eV):	-0.345056	-9.3894	Occ: 2.000000	Type:A+B
Orb:	57	Ene(au/eV):	-0.337746	-9.1905	Occ: 2.000000	Type:A+B
Orb:	58	Ene(au/eV):	-0.337733	-9.1902	Occ: 2.000000	Type:A+B
Orb:	59	Ene(au/eV):	-0.316458	-8.6112	Occ: 2.000000	Type:A+B
Orb:	60	Ene(au/eV):	-0.309852	-8.4315	Occ: 2.000000	Type:A+B
Orb:	61	Ene(au/eV):	-0.309843	-8.4313	Occ: 2.000000	Type:A+B
Orb:	62	Ene(au/eV):	-0.238168	-6.4809	Occ: 2.000000	Type:A+B
Orb:	63	Ene(au/eV):	-0.238165	-6.4808	Occ: 2.000000	Type:A+B
Orb:	64	Ene(au/eV):	-0.232604	-6.3295	Occ: 2.000000	Type:A+B
Orb:	65	Ene(au/eV):	-0.232601	-6.3294	Occ: 2.000000	Type:A+B
Orb:	66	Ene(au/eV):	-0.071009	-1.9323	Occ: 0.000000	Type:A+B
Orb:	67	Ene(au/eV):	-0.070994	-1.9318	Occ: 0.000000	Type:A+B
Orb:	68	Ene(au/eV):	-0.016728	-0.4552	Occ: 0.000000	Type:A+B
Orb:	69	Ene(au/eV):	-0.000287	-0.0078	Occ: 0.000000	Type:A+B
Orb:	70	Ene(au/eV):	0.007679	0.2090	Occ: 0.000000	Type:A+B
Orb:	71	Ene(au/eV):	0.007693	0.2093	Occ: 0.000000	Type:A+B
Orb:	72	Ene(au/eV):	0.056840	1.5467	Occ: 0.000000	Type:A+B

Note: Orbital 65 is HOMO, energy: -0.232601 a.u. -6.329405 eV

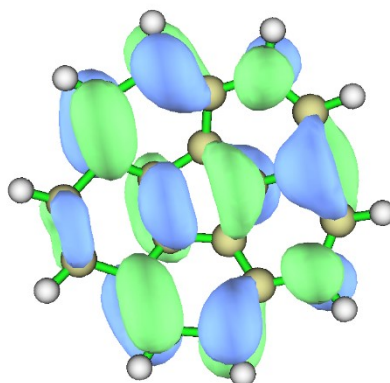
Orbital 66 is LUMO, energy: -0.071009 a.u. -1.932253 eV

HOMO-LUMO gap: 0.161592 a.u. 4.397151 eV 424.260709
kJ/mol

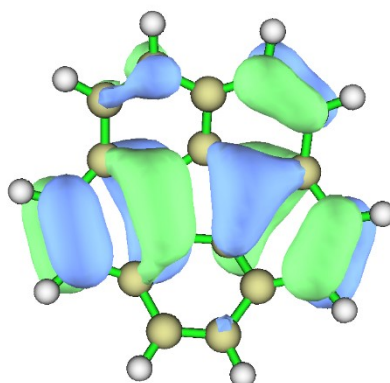
HOMO:



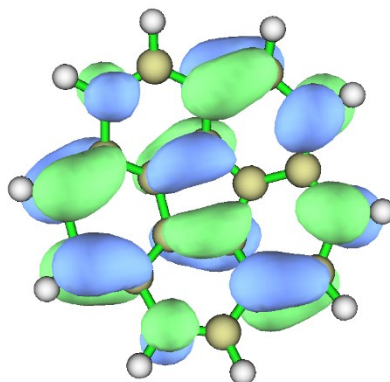
LUMO:



Orbital64:



Orbital67:



The pristine corannulene has a C_{5v} symmetry and shows quadruply degenerate HOMOs. The unoccupied orbitals begin with a doubly degenerate set of LUMOs. The principal transitions are π -to- π^* . The HOMO-LUMO energy gap was determined to be 4.40 eV. The above observations agree well to those obtained by Siegel et al.¹⁵

Interestingly, compound **1** breaks the C_{5v} symmetry, HOMO and LUMO orbitals loss the degeneracy, leading to a HOMO-LUMO energy gap of 3.51 eV. Symmetry-breaking causes a decrease in HOMO-LUMO energy gap, augment in emission peak wavelength and increase in PL quantum yield. These tendencies are very similar to those of 5,10,15,20-tetraphenyl-21H ,23H-porphine zinc (ZnTPP) and 5,10,15,20-tetraphenyl-21H ,23H -porphine (H₂TPP).¹⁶

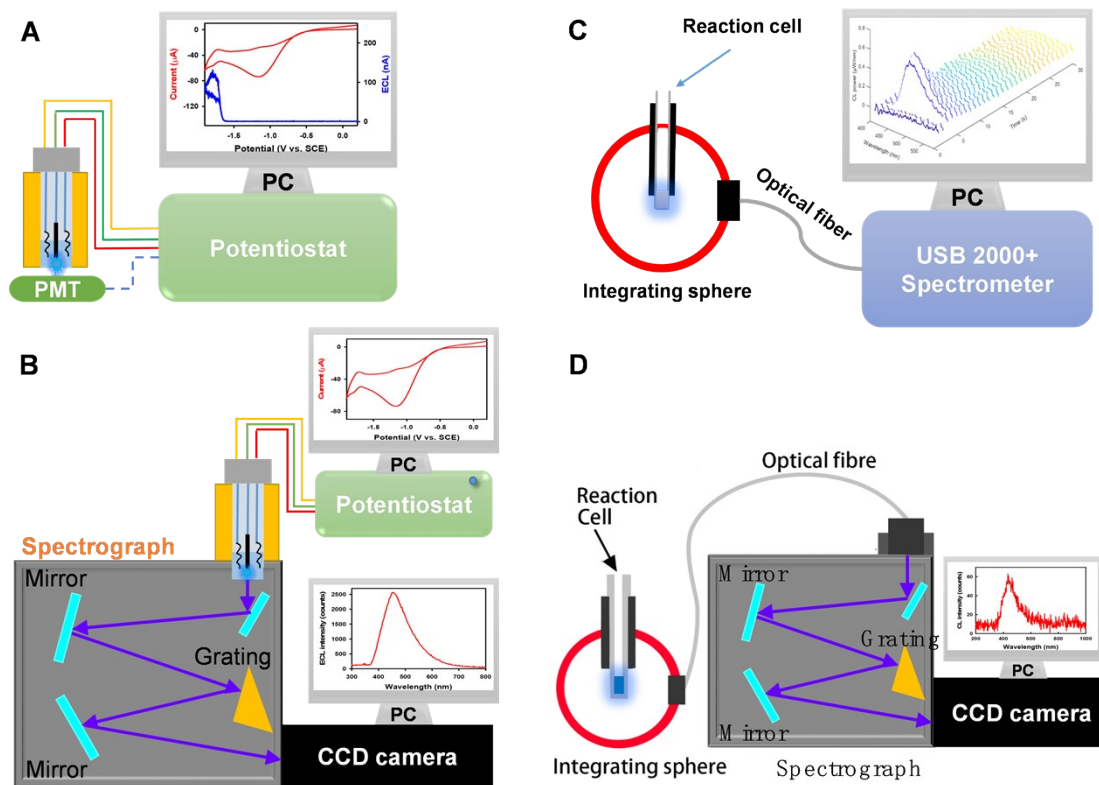


Figure S7. Illustrative instrumentation of (A, B) ECL and (C, D) CL experiments for measurements of absolute ECL (A) and CL (C) efficiencies as well as ECL (B) and CL (D) spectra.

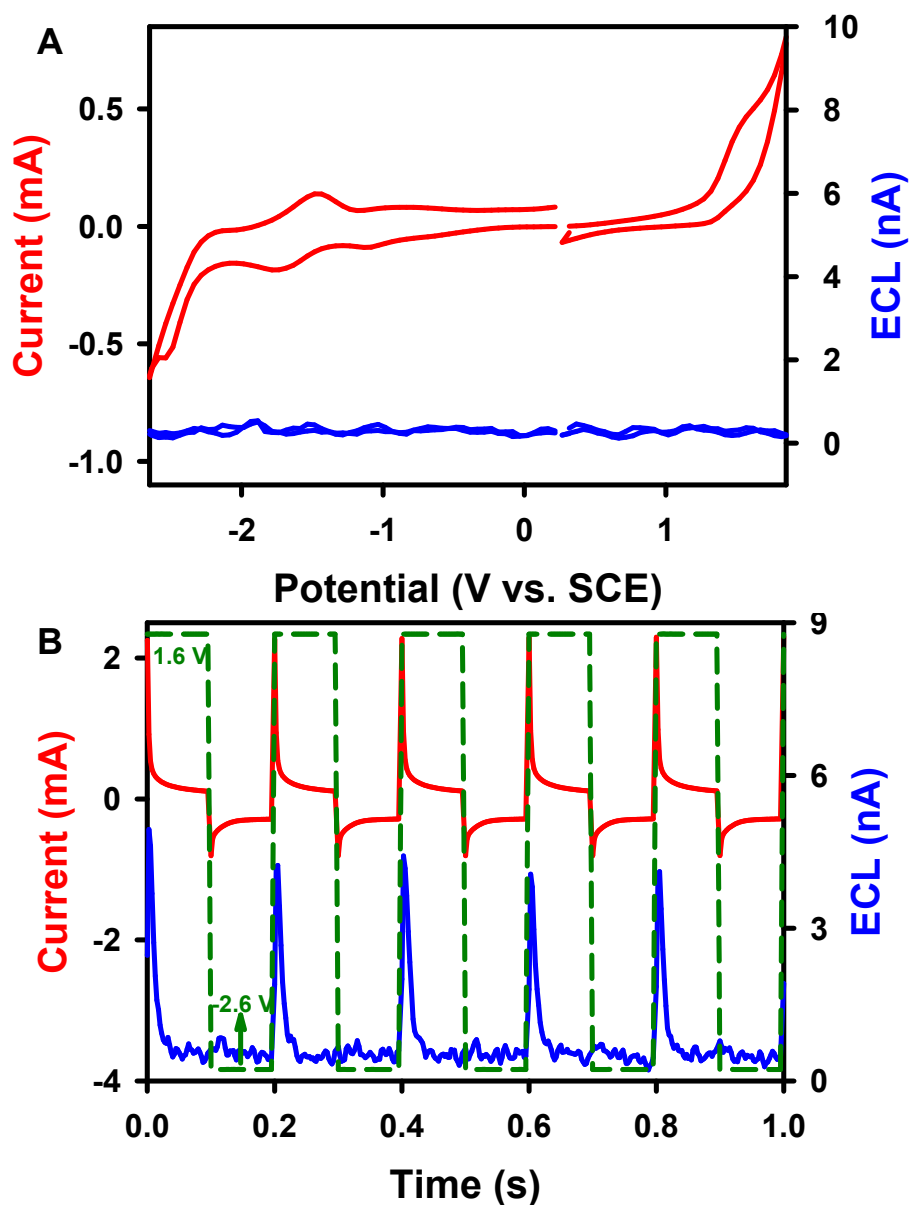


Figure S8. (A) CV with the ECL-voltage curve of 0.6 mM **Cor** in 1:1 benzene:MeCN (volume ratio) solution with 0.1 M TBAPF₆ as the supporting electrolyte. The CV scan rate was at 10 V s⁻¹. (B) The current-time response along with the corresponding ECL-time curve of 0.6 mM **Cor** 1:1 benzene:MeCN (volume ratio) solution with 0.1 M TBAPF₆ as the supporting electrolyte during a potential pulsing experiment between -2.60 and 1.60 V at a frequency of 10 Hz. The corresponding applied potentials are indicated in dashed green.

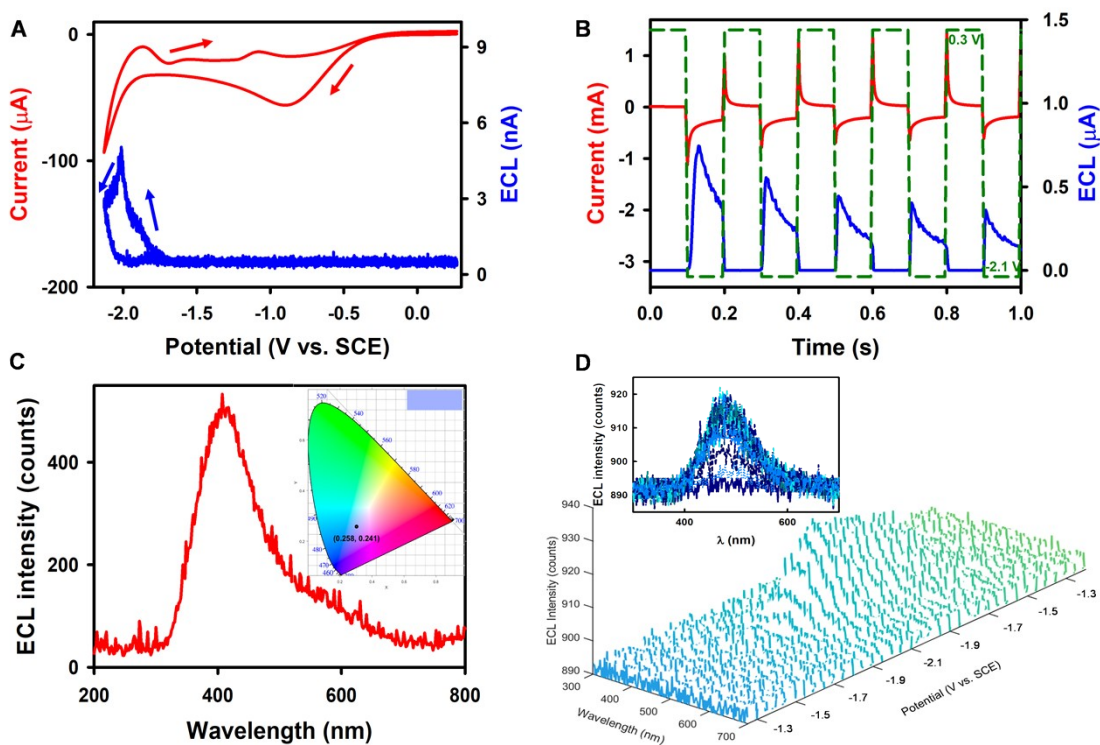


Figure S9. (A) Cyclic voltammogram with the corresponding ECL-voltage curve of 0.6 mM **Cor** in the presence of 5 mM BPO in 1:1 benzene:MeCN (volume ratio) solution with 0.1 M TBAPF₆ as the supporting electrolyte. (B) The current-time with the corresponding ECL-time curves of 0.6 mM **Cor** with 5 mM BPO as the coreactant during a potential pulsing experiment at 10 Hz frequency. (C) The accumulated ECL spectrum of the potential pulsing experiment. The inset is the CIE coordinate diagram of the ECL spectrum. (D) Spooling ECL spectra of 0.6 mM **Cor** in the presence of 5 mM BPO. Insets are 2D viewings of the spectra.

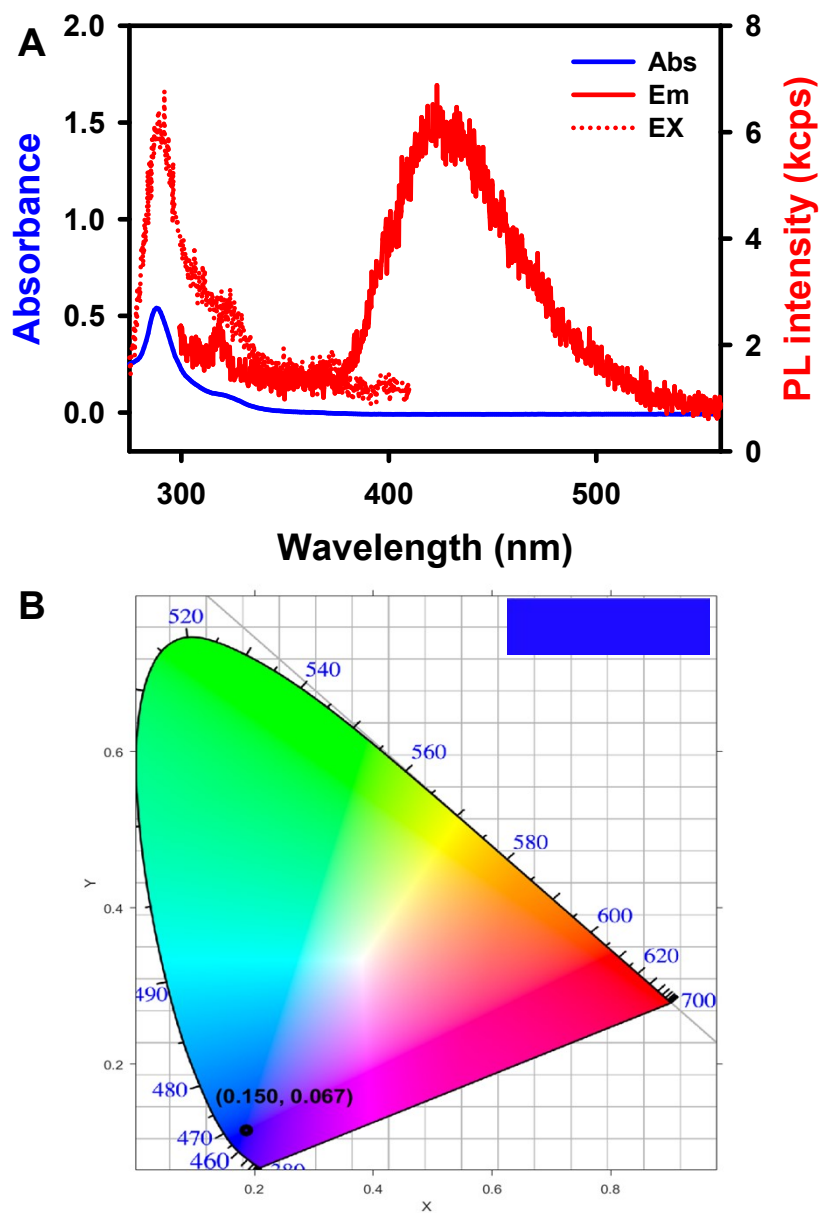


Figure S10. (A) UV-vis absorption and photoluminescence spectra of 10 μM Cor in 1:1 benzene:MeCN (volume ratio) solution, $\lambda_{\text{ex}} = 287$ nm and $\lambda_{\text{em}} = 421$ nm. (B) The CIE coordinate diagram of the PL spectrum.

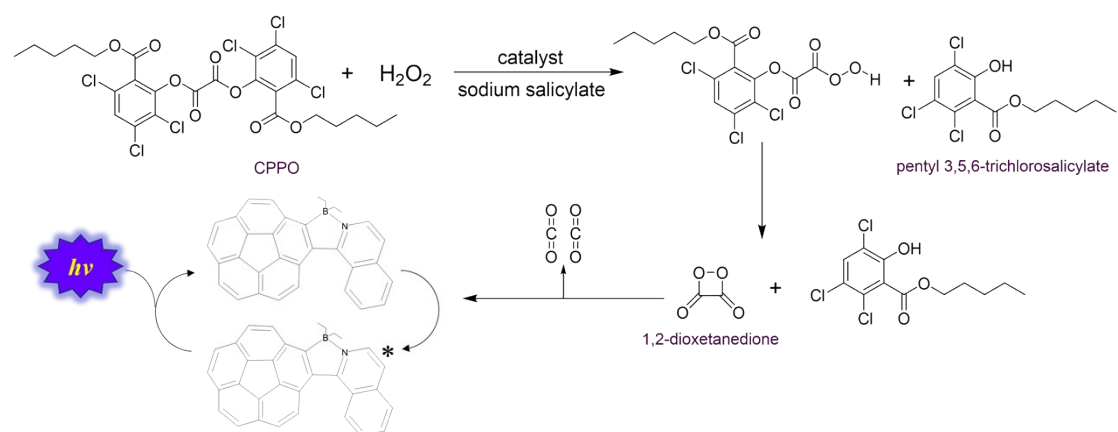


Figure S11. Reaction diagram of the peroxyoxalate-based CL reaction with CPPO and H_2O_2 reagents.

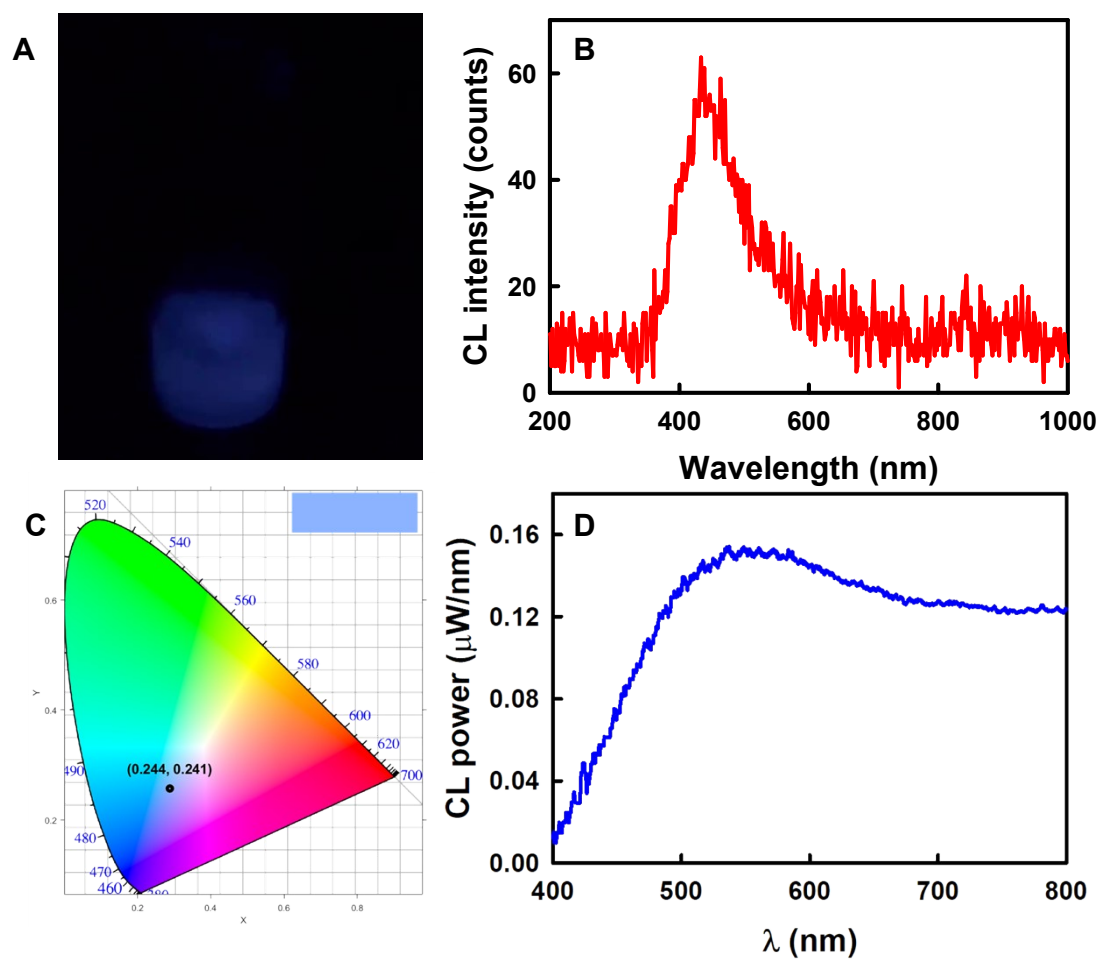


Figure S12. (A) Photograph of **Cor** in CL reaction solution. (B) CL spectra acquired at a time interval of 5 s in the presence of **Cor**, CPPO, and H_2O_2 . Conditions were: 1 mL of 30% H_2O_2 in acetonitrile added to 1 mL of an 80% DMF/20% acetonitrile solution containing 6 mg mL^{-1} **Cor**, 40 mg mL^{-1} CPPO, and 2 mg mL^{-1} sodium salicylate. (C) The CIE coordinate diagram of the CL spectrum. (D) The conversion curve of the μW as a function of the wavelength.

Table S1. Experimental photophysical properties in CH₂Cl₂^a

	λ_{max} (abs) ^b	ϵ_{max}	λ_{max} (em) ^c	Φ_f ^d	Stokes shift (nm)	Stokes shift (cm ⁻¹)
1	304, 342, 386, 407, 425	26300	447, 468	0.31	164	11527

^a Recorded in deoxygenated anhydrous dichloromethane. ^b Longest absorption maximum. ^c Emission maximum upon excitation at the longest absorption maximum. ^d Absolute quantum yield determined by calibrated integrating sphere systems.

¹H NMR Line-shape Analysis

The variable-temperature (VT) ¹H NMR (600 MHz) experiments were performed in a solution of azaborahelicene corannulene **1** in CD₂Cl₂. The field shifts of the ¹H NMR resonances for H_a, H_b, and CH₃ protons were observed and used to determine the coalescence temperature (T_c). Measurements of the rate constants (k) for the bowl and helix inversion processes of **1** were conducted by dynamic ¹H NMR line-shape simulations using the program MestReNova (Version 14.0.0). The Eyring equation, $\Delta G_c^\ddagger = -RT \ln(kh/k_B T)$, was used to calculate the ΔG_c^\ddagger values at coalescence temperature (T_c). The ΔH^\ddagger and ΔS^\ddagger values were obtained through an Eyring plot ($1/T$ against $\ln(k/T)$, Figure S17) that was generated using rate constants (k) determined by dynamic ¹H NMR line-shape simulations (Figures S15 and S16). The equation, $\Delta G^\ddagger = \Delta H^\ddagger - T\Delta S^\ddagger$, was used to calculate the ΔG_{298K}^\ddagger values at room temperature (298 K).

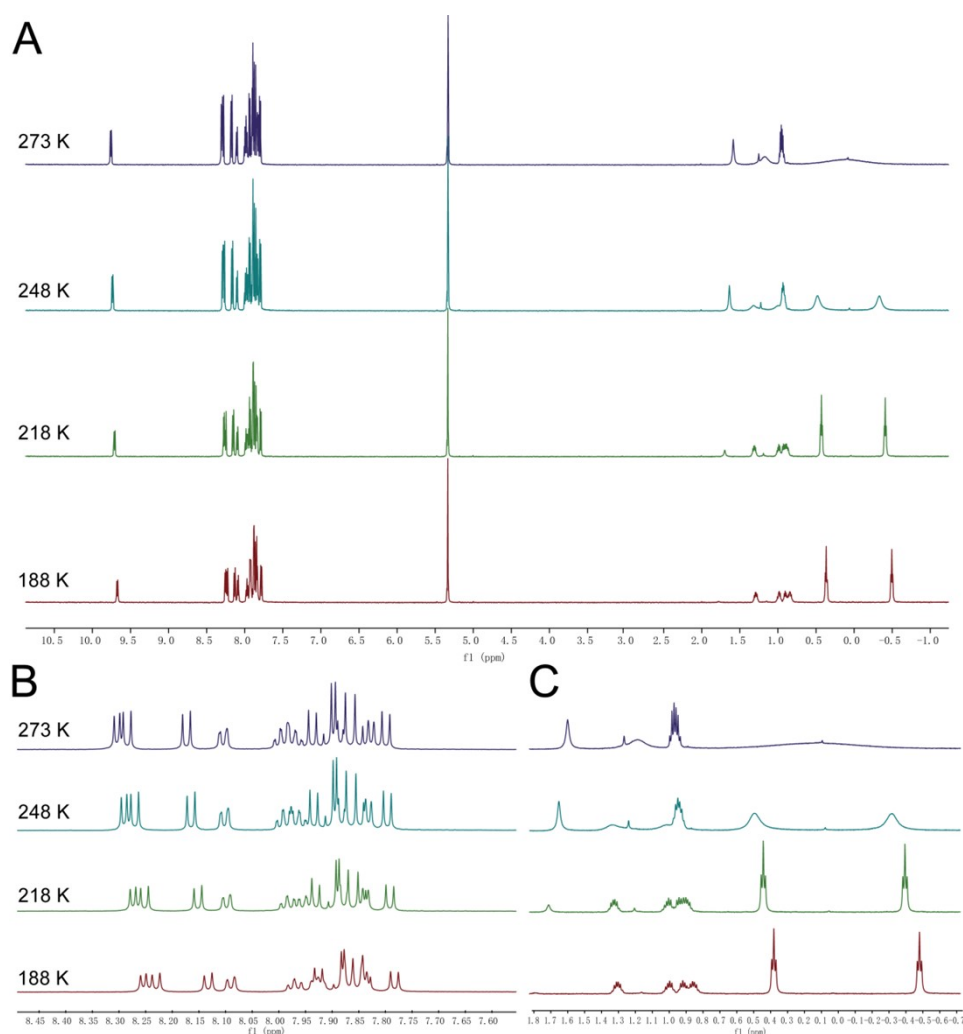


Figure S13 (A) Stacked ¹H NMR spectra of **1** acquired upon heating back to 273 K from 188

K with 30 K increments (600 MHz, CD₂Cl₂). (B) Spectra displaying the regions between 7.6 and 8.4 ppm. (C) Spectra displaying the regions between -0.7 and 1.8 ppm.

¹H NMR Line-Shape Analysis / CD₂Cl₂ / 600 MHz

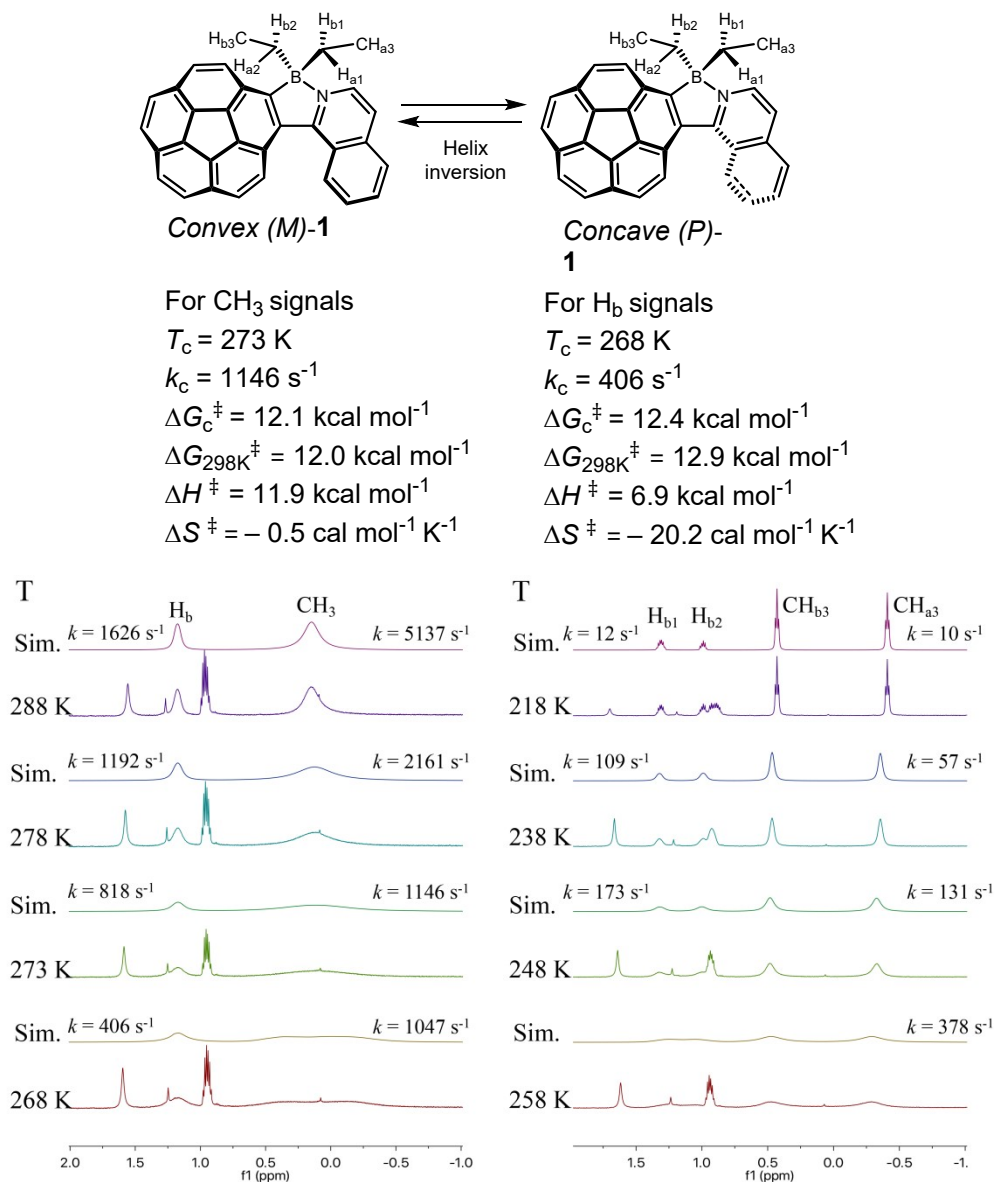


Figure S14 ¹H NMR line-shape simulations for helix inversion process of compound **1** in CD₂Cl₂. T = temperature, k = rate constant, and Sim. = simulated. The coalescence temperatures (T_c) are estimated at 273 K for CH₃ and 268 K for H_b. The energy barriers ΔG_c^\ddagger for helix motif inversion are experimentally found to be 12.1 kcal mol⁻¹ for CH₃ signals and 12.4 kcal mol⁻¹ for H_b signals at coalescence temperatures. ΔG_{298K}^\ddagger values at room temperature are calculated to be 12.0 kcal mol⁻¹ for CH₃ signals and 12.9 kcal mol⁻¹ for H_b signals. $\Delta G_{298K}^\ddagger = 12.0$ kcal mol⁻¹ is used for

energy barrier of helix motif inversion because helix inversion is more sensitive to changing chemical environment and better-fitted to the Eyring plot (Fig. S16B-C).

¹H NMR Line-Shape Analysis / CD₂Cl₂ / 600 MHz

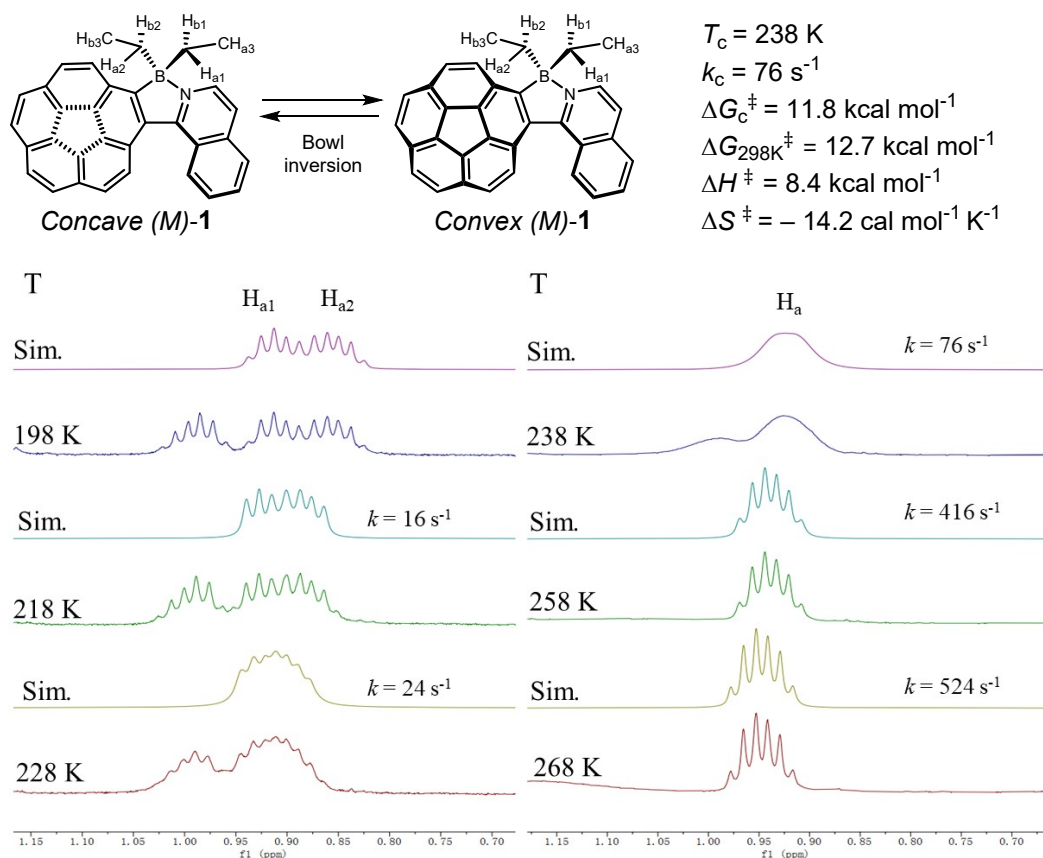


Figure S15 ¹H NMR line-shape simulations for bowl inversion process of compound **1** in CD₂Cl₂. T = temperature, *k* = rate constant, and Sim. = simulated. The coalescence temperature (*T_c*) is estimated at 238 K for H_a, and the energy barrier ΔG_c^\ddagger for corannulene motif inversion is experimentally found to be 11.8 kcal mol⁻¹ at the coalescence temperature (*T_c* = 238 K) (Fig. S16A). $\Delta G_{298\text{K}}^\ddagger$ value at room temperature (298K) are calculated to be 12.7 kcal mol⁻¹ for H_a signals.

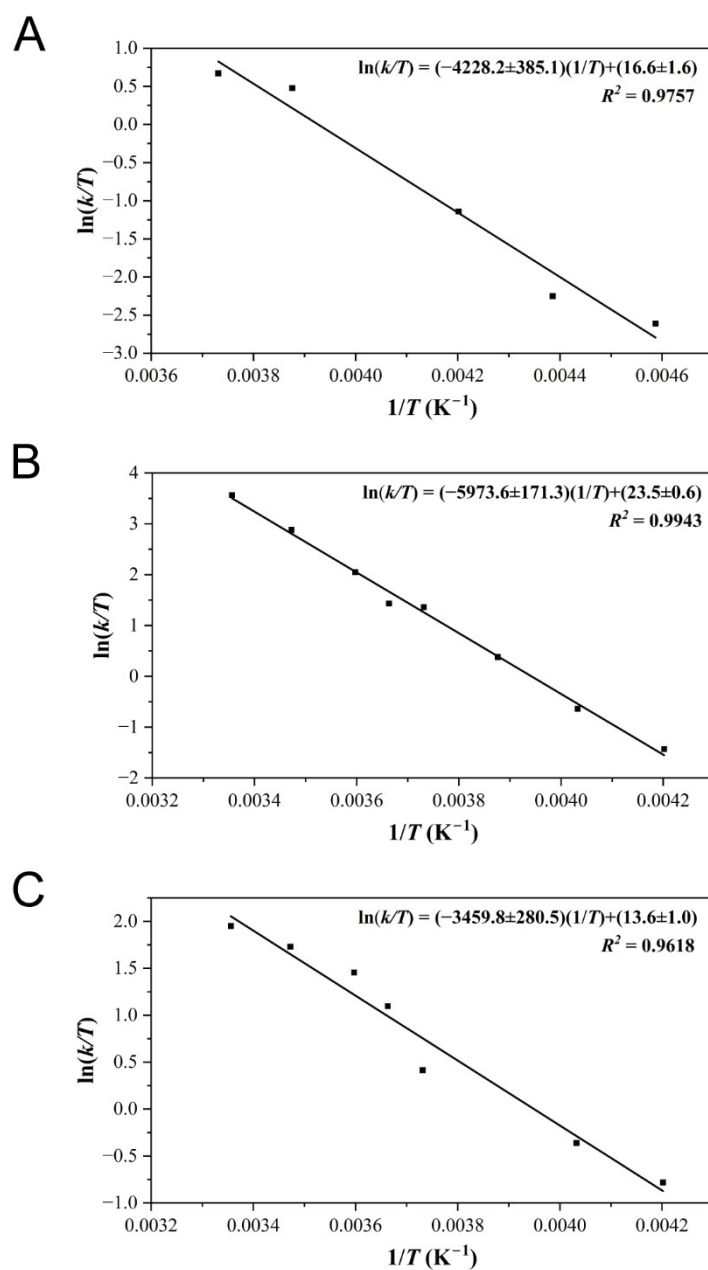


Figure S16 Eyring plots for (A) bowl inversion (Signals from H_a protons), $\Delta H^\ddagger = 8.4$ kcal mol⁻¹, $\Delta S^\ddagger = -14.2$ cal mol⁻¹ K⁻¹. (B) helix inversion (Signals from CH₃ protons), $\Delta H^\ddagger = 11.9$ kcal mol⁻¹, $\Delta S^\ddagger = -0.5$ cal mol⁻¹ K⁻¹. (C) helix inversion signals from H_b protons). $\Delta H^\ddagger = 6.9$ kcal mol⁻¹, $\Delta S^\ddagger = -20.2$ cal mol⁻¹ K⁻¹. $\Delta H^\ddagger = -R \times (\text{solpe})$. $\Delta S^\ddagger = R \times (\text{intercept} - 23.76)$.

More detail on ¹H NMR analysis

The chemical shift for hydrogens in two CH₃ is easily identified by integral of the peak intensity

in room-temperature NMR spectrum such as the one in Figure S3 in ESI, while it was found that there are two types of hydrogens, Ha and Hb, with different chemical environments as demonstrated in Figure 9 of the paper. Through VT-NMR spectroscopy, it is plausible that Ha is in the vicinity of the bowl (relatively low chemical shift) while Hb in the proximity of the helicene (relatively high chemical shift), as labeled in Figures 9 in the paper and Figure S17 below.

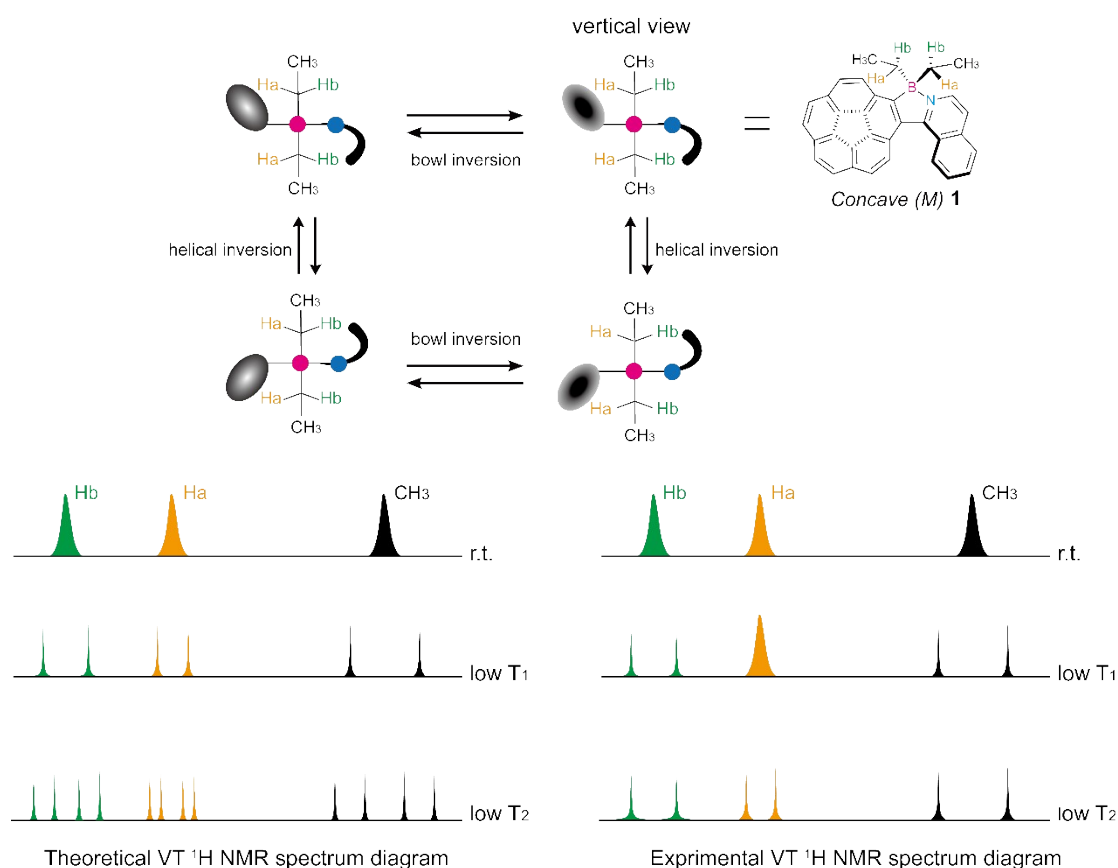


Figure S17: Simplified sketch map of compound **1**'s inversion pathways from vertical view (top), and VT ¹H NMR spectra diagram (bottom).

As illustrated in Figure 8 in the paper, the Ha/Hb signals for different diastereomers of compound **1**, resulting from both bowl and helical inversions, are expected to display distinct hydrogen signals with varying chemical shifts in the low-temperature ¹H NMR spectra. In theory, eight CH₂ (Ha & Hb) proton signals and four CH₃ proton signals should be observed in low temperature ¹H NMR spectra, lower left in Figure S17 above. However, only two Ha signals, two Hb signals, and two CH₃ signals, situated in different chemical environments, were observed in ¹H NMR spectrum at -85 °C (Figure 9 in the paper), indicating distinct effects of bowl and helicene inversions on the chemical environments of aliphatic hydrogens.

Interestingly, depending on the rate of bowl and helicene inversion processes in compound **1**

on the NMR timescale, Hb and CH₃ signals split into two sets of signals at 273 K, whereas Ha signals split into two sets of signals at a different temperature (238 K), as demonstrated in Figure 9 of the paper. The most plausible explanation is that the stereoisomerism caused by helical inversion (P/M isomers) predominantly influences the chemical environments of Hb and CH₃ hydrogens, while the effects of stereoisomerism due to bowl inversion (*convex/concave* isomers) are negligible. The situation is precisely the reverse for Ha. In literature, Scott et al¹⁷ utilized dimethylcarbinol and Siegel et al¹⁸ used ethyl to probe corannulene bowl-to-bowl inversion. For the first time, we employed Hb and CH₃, Ha to probe the inversions of both the bowl and helicene.

In details, as shown in Figure 8 in the paper, the bowl and helicene inversions of compound **1** are rapid at room temperature, resulting in only three types of proton signals (Ha, Hb, and CH₃) observed in the ¹H NMR spectra. As the temperature decreases, the dynamic inversion rates of compound **1** begin to slow down. In theory as illustrated on the lower left panel of Figure S17, when the helical inversion reaches the NMR timescale at a certain temperature (T₁), the diastereomers can be detected by ¹H NMR, and the proton signals (Ha, Hb, and CH₃) might start to split into two sets for each of the three peaks. As the temperature continues to decrease to T₂, the remaining bowl inversion reaches the NMR timescale, causing the initially split six sets of peaks to further divide into twelve sets of proton signal peaks. This is the phenomenon that should theoretically be observed (lower left of Figure S17), but in reality, it is as shown in the lower right of Figure S17 at T₁, only the Hb and CH₃ hydrogen signals undergo splitting. When the temperature drops to T₂, the Ha peak splits, while the Hb and CH₃ hydrogen signals remain unchanged. The plausible explanation is that the stereoisomerism caused by helical inversion (P/M isomers) and bowl inversion (*convex/concave* isomers) differentially influences the chemical environments of the Ha, Hb, and CH₃ protons. As the Hb and CH₃ signals are in closer spatial proximity to the helix motif and exhibit nearly identical coalescence temperatures (T₁, ~273 K), they are strongly supposed to be affected by helical inversion, while the Ha signal shows a significantly lower coalescence temperature (T₂, 238 K) and situates near the corannulene motif, which is expected to be affected by bowl inversion. These above enable the observations of both bowl and helical inversion processes of compound **1** affecting different proton signals in the VT ¹H NMR spectra.

References

1. Y. Wang, H. Jiang, X. Liu, J. Xu, Y. Gao and N. S. Finney, *Chem. Commun.*, 2021, **57**, 5818-5821.
2. L. Yang, A. D. Hendsbee, Q. Xue, S. He, C. R. De-Jager, G. Xie, G. C. Welch and Z. Ding, *ACS Appl. Mater. Inter.*, 2020, **12**, 51736-51743.
3. X. Qin, L. Yang, X. Wang, D. Patel, K. Chu, L. Kelland, J. R. Adsetts, C. Zhang, M. S. Workentin, B. L. Pagenkopf and Z. Ding, *ChemElectroChem*, 2022, **9**, e202200605.
4. Z. Zhan, X. Qin, K. Chu, X. Sun and Z. Ding, *J. Electroanal. Chem.*, 2023, **932**, 117220.
5. M. Hesari and Z. Ding, *Nat. Protoc.*, 2021, **16**, 2109-2130.
6. X. Qin, Z. Zhan, R. Zhang, K. Chu, Z. Whitworth and Z. Ding, *Nanoscale*, 2023, **15**, 3864-3871.
7. J. R. Adsetts, K. Chu, M. Hesari, J. Ma and Z. Ding, *Anal. Chem.*, 2021, **93**, 11626-11633.
8. L. Yang, J. R. Adsetts, R. Zhang, B. Balónová, M. T. Piqueras, K. Chu, C. Zhang, E. Zysman-Colman, B. A. Blight and Z. Ding, *J. Electroanal. Chem.*, 2022, **906**, 115891.
9. M. M. Rauhut, L. J. Bollyky, B. G. Roberts, M. Loy, R. H. Whitman, A. V. Iannotta, A. M. Semsel and R. A. Clarke, *J. Am. Chem. Soc.*, 1967, **89**, 6515-6522.
10. A. Eghlimi, H. Jubaer, A. Surmiak and U. Bach, *J. Chem. Educ.*, 2019, **96**, 522-527.
11. M. Rauhut, D. Sheehan, R. Clarke, B. Roberts and A. Semsel, *J. Org. Chem.*, 1965, **30**, 3587-3592.
12. M. M. Rauhut, B. G. Roberts and A. M. Semsel, *J. Am. Chem. Soc.*, 1966, **88**, 3604-3617.
13. G. M. Sheldrick, *Acta Crystallogr. C Struct. Chem.*, 2015, **71**, 3-8.
14. O. V. Dolomanov, L. J. Bourhis, R. J. Gildea, J. A. K. Howard and H. Puschmann, *J. Appl. Crystallogr.*, 2009, **42**, 339-341.
15. Y.-T. Wu, D. Bandera, R. Maag, A. Linden, K. K. Baldrige and J. S. Siegel, *J. Am. Chem. Soc.*, 2008, **130**, 10729-10739.
16. R. Zhang, A. Zhang, M. J. Stillman and Z. Ding, *J. Phys. Chem. C*, 2020, **124**, 16568-16576.
17. L. T. Scott, M. M. Hashemi and M. S. Bratcher, *J. Am. Chem. Soc.*, 1992, **114**, 1920-1921.
18. M. Juriček, N. L. Strutt, J. C. Barnes, A. M. Butterfield, E. J. Dale, K. K. Baldrige, J. F. Stoddart and J. S. Siegel, *Nat. Chem.*, 2014, **6**, 222-228.